PCCP

PAPER

View Article Online
View Journal | View Issue

Cite this: *Phys. Chem. Chem. Phys.*, 2018, **20**, 4129

Transition states of spin-forbidden reactions†

Bo Yang, *[abc] Laura Gagliardi *[abc] and Donald G. Truhlar *[abc]

Received 25th October 2017,
Accepted 3rd January 2018

DOI: 10.1039/c7cp07227a

rsc.li/pccp

Spin–orbit coupling plays an important role in determining the mechanisms and kinetics of spin-forbidden reactions and many reactions exhibiting two-state reactivity. Spin–orbit coupling can allow the system to change its spin state, especially when potential energy surfaces (PESs) of two spin states approach each other. Here, we introduce a convenient new approximation method for locating stationary points on the lowest mixed-spin potential energy surface along a reaction pathway by using density functional calculations. The mixing of different spin states is achieved by introducing the spin–orbit coupling into the electronic Hamiltonian using a pre-defined coupling constant. Two examples are given using the new methodology: (a) a CO association reaction with the coordinatively unsaturated $Fe(CO)_4$ complex and (b) an α-H elimination reaction of a model complex containing W. We computed a Gibbs free energy of activation of 2.8 kcal mol^{-1} for the CO association reaction, which is reasonably consistent with the experimentally measured reaction rate. For the H elimination reaction, the spin change occurs at a relatively low energy, and the present treatment allows one conclude that kinetics of the reaction can be reasonably well described without spin–orbit coupling.

1. Introduction

Computational quantum chemistry has become increasingly successful in guiding the experimental investigation of organometallic chemistry.[1,2] Spin-forbidden reactions are quite common among the many reactions that involve transition metals, but computational methods are not as convenient or well developed as for spin-conserving reactions.[3,4] The chemistry of transition metal compounds is mainly controlled by the valence d-orbital electrons on the metal center. Uncoordinated transition metal atoms and those coordinated with weak-field ligands usually prefer high-spin configurations with unpaired electrons in the d-orbitals. In the presence of strong-field ligands, however, the d-orbitals can split enough that one has a lower-spin configuration. For many organometallic compounds, the d-orbital splitting caused by a ligand field is moderate, and high- and low-spin configurations lie relatively close in energy. In a chemical reaction, the change in ligand field around the metal may have the effect that the ground state of the products has a different spin state than that of the reactants.

Experimental studies have revealed many reactions in which reactants and products are dominated by different spin states.[5] The spin–orbit coupling between the two spin states allows the wave functions of different spin states to mix, and this mixing is especially strong when a system reaches a geometry where the potential energies of two spin states are nearly equal. Transition metals, especially those in the second and the third transition rows, usually exhibit strong spin–orbit coupling.[6,7] A spin-changing reaction can be faster or slower or have the same rate as the corresponding spin-conserving one,[8] and quantitative calculations may be required to determine which mechanism dominates. The mechanistic role of spin change during a reaction mainly depends on (i) the amount of energy needed for the system to reach a configuration where the potential energies of two spin states are close, and (ii) the magnitude of spin–orbit coupling between two spin states. If the stationary geometries of different spin states are significantly different, the energy required for their potential energies to approach each other can be quite large, and so the process leading from one spin state to the other can be very slow, even if the spin–orbit coupling is strong.

The difficulty of determining the kinetics of spin-changing reactions mainly arises from the need for complicated electronic structure calculations in which spin–orbit coupling[9] is included. As a result, many studies focus on acquiring qualitative information near the crossing region by calculating single-point energies

[a] *Department of Chemistry, University of Minnesota, Minneapolis, Minnesota, 55455-0431, USA. E-mail: yang3227@umn.edu, gagliard@umn.edu, truhlar@umn.edu*
[b] *Chemical Theory Center and Minnesota Supercomputing Institute, University of Minnesota, Minneapolis, Minnesota, 55455-0431, USA*
[c] *Inorganometallic Catalyst Design Center, University of Minnesota, Minneapolis, Minnesota, 55455-0431, USA*

† Electronic supplementary information (ESI) available: (a) Details of evaluating the spin–orbit coupling parameter χ. (b) DFT-optimized stationary point geometries and energies on the lowest mixed-spin potential energy surface along the reaction coordinates for: (1) CO association reaction with the coordinatively unsaturated $Fe(CO)_4$ complex, (2) α-H elimination reaction over a W model complex. See DOI: 10.1039/c7cp07227a

on one potential energy surface at stationary points or other important points on the other potential energy surface.[10–12] Such calculations only provide an approximation to the activation barrier of the reaction, but under the assumption that potential energy surfaces are relatively smooth and the geometrical parameters do not depend strongly on spin state, such calculations can provide useful information about the region where the crossing will occur.

A considerable amount of theoretical work focuses on locating the geometry of the lowest energy at which different spin state surfaces cross. The method of partial optimization[13,14] predefines a reaction coordinate (*e.g.*, a bond length or bond angle) and then performs partial geometry optimization on potential energy surfaces (PESs) of different spin states at a fixed set of values of the chosen coordinate. More precise methods for locating the minimum energy crossing point (MECP) along the reaction pathway have been described by several groups.[15–23] Although it is neglected in the above treatments, in reality, the spin–orbit coupling yields a mixed-spin adiabatic state with a lower energy than the energy of the two uncoupled states at their lowest-energy crossing, so it is unsatisfactory that all the above methods consider only the PESs of two spin states without considering any effect of spin–orbit coupling. Furthermore, the saddle point on the mixed-spin true ground state may differ considerably from the geometries examined on the basis of neglecting spin–orbit coupling.

We here mention some alternative methods for treating this kind of problem. Kim *et al.*,[24] used CASSCF-RASSI-SO[25] to optimize the minimum energy crossing point of a doublet and a quartet surface, followed by a single-point CASPT2-RASSI-SO[26] to add external correlation. This method is more expensive than that proposed here, and it has the disadvantage that the geometries of the MECP and the saddle pint can differ significantly when SOC is large and optimized geometries can differ significantly when optimized with and without external correlation. In a later study Kim *et al.*[27] used spin–orbit multiconfigurational quasi-degenerate perturbation theory (SO-MCQDPT)[28] to calculate external correlation energy and SO coupling along reaction paths calculated by DFT. Gaggioli *et al.*[29,30] optimized spin-coupled transition structures using noncollinear DFT[31,32] with the spin–orbit ZORA Hamiltonian.[31] The DFT-ZORA-SO method can be applied to much larger systems.

The present work provides a simple approximation for finding the barrier for spin-changing reactions that explicitly includes the spin–orbit coupling and optimizes the saddle point on an approximate mixed-spin surface at low cost. The effect of spin–orbit coupling is included in an approximate way in the Hamiltonian used for optimization by using a spin–orbit coupling constant defined prior to the calculation to avoid the complexity and cost of higher-level approximations. With the inclusion of the spin–orbit coupling in the scanning of the potential energy surface, the system can evolve from geometries dominated by one spin state to those dominated by another. We will call the new method the two-state spin-mixing model (TSSMM), and the calculations are performed by a Perl script called TSSMM.

2. Theory

In the case where the low-spin state is energetically more stable than the high-spin state for reactants and less stable for products, the lowest mixed-spin state will have a mainly low-spin character on the reactant side of the reaction path and mainly high-spin character on the product side. Due to spin–orbit coupling, the saddle point on the lowest mixed-spin PES will have lower energy than any point on the crossing seam where low- and high-spin PESs intersect. The saddle point geometry or the mixed-spin system, which is the highest-energy point on the lowest-energy path from reactants to products, can be determined if the energy of the lowest mixed-spin state can be calculated as a function of geometry. The result is the conventional transition structure (lowest-energy point of the transition state hypersurface) for the reaction on the lowest spin–orbit-coupled (spin-mixed) potential energy surface.

If the PESs are obtained by diagonalizing the electronic Hamiltonian in a system with an even number of electrons or a system excluding the spin–orbit coupling terms, the individual spin states intersect on an $(F - 2)$-dimensional space if they have the same spin and electronic symmetry and on an $(F - 1)$-dimensional seam if they have different spins or different electronic symmetries, where F is the number of nonredundant degrees of freedom ($F = 3N - 6$, where N is the number of atoms). Upon including spin–orbit coupling in the Hamiltonian for a system with an odd number of electrons, we get mixed-spin PESs that cross on an $(F - 5)$-dimensional seam[33] (although crossing might occur in higher dimensionality in an approximate theory[34,35]). In calculating reaction barrier heights, though, we need not be concerned with actual intersections because the saddle point will be located on the side of an intersection.[36–38]

The multiplicity of a state of spin S is $2S + 1$, so a full treatment of spin–orbit coupling inevitably involves more than two states. However, as emphasized by Granucci *et al.*[39] and Cui and Thiel,[40] "the total intermultiplet transition probability between two states of different spin should be rotationally invariant". This can be achieved by assuming that each spin multiplet can be considered as a single electronic state when the strength of coupling between states of different spins changes slowly with the change of nuclear coordinates and the derivative coupling between electronic states of a spin multiplet be neglected.[39,40] As discussed elsewhere in the context of singlet–triplet mixing,[41] it is reasonable to replace the three triplet states by a single state that is coupled by the norm of the spin–orbit coupling if the spin–orbit coupling is small. This approximation is widely used.[40,42] This is particularly convenient in that it reduces the problem to a two-state configuration interaction (CI). The diagonal elements of the 2×2 Hamiltonian are the energies of the low- and high-spin states, which can be determined conventionally through Kohn–Sham SCF calculations. (Note that Kohn–Sham determinants sometimes suffer from large spin contamination, and the method should be used with appropriate caution.) The remaining problem is the evaluation of the off-diagonal elements. The most

important of these terms, for our purposes, is the spin–orbit coupling. While this could be obtained from *ab initio* calculations such as complete active space state-interaction (CASSI) calculations,[26,40,43,44] in the present article we propose a simpler alternative.

This alternative is to evaluate spin–orbit coupling by a model space approach involving two effective states coupled by a semiempirical constant spin–orbit coupling term, χ, which we refer to as the coupling constant and which is used as an off-diagonal Hamiltonian element:

$$H = \begin{pmatrix} E_1 & \chi \\ \chi & E_2 \end{pmatrix} \quad (1)$$

where E_1 and E_2 are the energies of low- and high-spin states for the given geometry. The coupling constant may be chosen semiempirically to reproduce the multiplet splitting in the atom or monatomic ion,[6,45,46] but one can also determine the constant by a time-dependent density-functional theory (TDDFT) or a CASSI calculation at a representative geometry along the reaction coordinate where the low- and high-spin surfaces are close in energy, and this is what was done in the present work by using TDDFT. An alternative is to replace χ with the geometry-dependent matrix element of a one-electron operator that has a parameter adjusted to reproduce the multiplet splitting in the atom or monatomic ion.[47]

3. Computational methods

A Perl script, called TSSMM,[48] was developed that interfaces with either the Gaussian 09[49] or Gaussian 16[50] program for the purpose of locating the stationary points on the lowest spin–orbit coupled PES. The geometry optimization is achieved by using the Gaussian optimizer and providing it with energies and corresponding derivatives that are calculated within the Perl script using the pre-defined coupling constant introduced above. In our calculation, the coupling constant, which is reaction specific, is chosen prior to the geometry optimization to reproduce the multiplet splitting at a representative geometry. Where the two spin states are close in energy.

The singlet–triplet excitation energies are determined by a relativistic TDDFT calculation using the ADF 2016 program.[51–55] The effect of spin–orbit coupling is included self-consistently by using the two-component zeroth-order regular approximation (ZORA).[55–59] Details of locating the representative geometry and calculating the coupling constants are provided in the ESI.†

As in as all Kohn–Sham calculations, the accuracy of the result depends on the choice of exchange–correlation functional and basis set. In this work, all calculations are carried out using the unrestricted (*i.e.*, spin-polarized) formalism with the M06-L[58] local density functional. M06-L shows particularly high accuracy for transition metal chemistry.[59,60] Details about the basis sets used in each calculation are provided within the context of each example discussed in Section 4.

The geometry optimization is performed by iterating the following three steps until convergence criteria are met:

(a) Two single-point density functional calculations for a given geometry (one for the low-spin state and one for the high-spin state) using the Gaussian program. The resulting energies and gradients of the spin states are provided to the TSSMM Perl script at the end of the two calculations.

(b) The TSSMM script calculates the energy, gradient, and Hessian of the mixed-spin state by the following equations under the assumption that the spin–orbit coupling term, χ, is constant:

$$E_{\text{mixed}} = \min\left\{\text{eigenvalue}\begin{pmatrix} E_1 & \chi \\ \chi & E_2 \end{pmatrix}\right\} \quad (2)$$

$$G_{\text{i}} \equiv \frac{\partial E_{\text{mixed}}}{\partial q_{\text{i}}} = \frac{(1-A)}{2}\frac{\partial E_1}{\partial q_{\text{i}}} + \frac{(1+A)}{2}\frac{\partial E_2}{\partial q_{\text{i}}} \quad (3)$$

$$A = \frac{(E_1 - E_2)}{\sqrt{4\chi^2 + (E_1 - E_2)^2}}$$

$$H_{\text{ij}} \equiv \frac{\partial^2 E_{\text{mixed}}}{\partial q_{\text{i}}\partial q_{\text{j}}} = B_{\text{i,j}} + \frac{(1-A)}{2}\frac{\partial^2 E_1}{\partial q_{\text{i}}\partial q_{\text{j}}} + \frac{(1+A)}{2}\frac{\partial^2 E_2}{\partial q_{\text{i}}\partial q_{\text{j}}} \quad (4)$$

$$B_{\text{i,j}} = \frac{(A^2-1)\left(\frac{\partial E_1}{\partial q_{\text{i}}} - \frac{\partial E_2}{\partial q_{\text{i}}}\right)\left(\frac{\partial E_1}{\partial q_{\text{j}}} - \frac{\partial E_2}{\partial q_{\text{j}}}\right)}{2\sqrt{4\chi^2 + (E_1 - E_2)^2}}$$

(c) One step of geometry optimization is carried out using the chosen Gaussian optimizer based on the energies and derivatives provided by TSSMM in step (b). The updated geometry is then provided to TSSMM, and steps (a)–(c) are repeated.

Note that in these equations, the energies (E_1 and E_2) and their gradients are functions of geometry and are updated by new electronic structure calculations at every iteration as the geometry is optimized. The Hessians of E_1 and E_2 are also functions of geometry, and whether they are is updated at every iteration depends on which optimizer is used.

One has to be cautious when applying the method for systems where only light atoms are involved, for which the coupling constant can be small and any small geometric deviation from the crossing point will result in the system losing its mixed-spin nature and bring difficulty for locating the saddle point geometry.

To assure consistency, all calculations are performed without density fitting.

4. Results and discussion

We will give two applications.

4.1 CO dissociation reactions of the $Fe(CO)_n$ Complexes

Ligand association and dissociation are common reaction types that involve a change in the coordination structure of the metal atom. This leads to a change of the ligand field, and so the reaction may be accompanied by a change in spin state. The gas phase associations/dissociations of CO molecules with coordinatively unsaturated $Fe(CO)_n$ complexes, are good examples of such processes, as first reported by Seder *et al.*:[61]

$$Fe(CO)_2 + CO \rightarrow Fe(CO)_3 \quad (R1)$$

$$Fe(CO)_3 + CO \rightarrow Fe(CO)_4 \quad (R2)$$

$$Fe(CO)_4 + CO \rightarrow Fe(CO)_5 \quad (R3)$$

The reported reaction rates for the first two of the three reactions are about 10^{13} cm^3 mol^{-1} s^{-1}, which are essentially the rate of collision, whereas the third reaction is ~500 times slower.[61]

This difference in reaction rate was attributed to a spin change between the reactants and the product in reaction (R3). It was noted that $Fe(CO)_{2-4}$ have triplet ground states, whereas $Fe(CO)_5$ has a singlet ground state. As a result, the first two reactions are spin-allowed, whereas the third is spin-forbidden.

Therefore, we used the new method presented here to study the reaction of CO with triplet $Fe(CO)_4$ to form singlet $Fe(CO)_5$. The calculations are performed using the def2-TZVPP basis set[62,63] for all atoms. The coupling constant χ was set equal to 231.6 meV. (Details of how χ was approximated are provided in the ESI.†)

A saddle point was found on the mixed-spin surface with an Fe–C distance of 2.68 Å with the incoming CO approaching the $Fe(CO)_4$ complex within the equatorial plane of a bipyramidal structure. Fig. 1 shows front and side views of the optimized saddle point geometry. Detailed geometric parameters for the saddle point geometry (Fig. 3) are summarized in Table 1 along with the crossing-point geometries acquired using TSSMM and MECP packages for comparison purposes. The corresponding optimized structure coordinates are provided in the ESI.† The optimized saddle point geometry has one imaginary frequency of 97i cm^{-1}. To further confirm that the optimized saddle point geometry is the desired transition structure that connects the reactant ($Fe(CO)_4$ + CO) and the product ($Fe(CO)_5$), we calculated the minimum energy path (MEP) using the IRC keywords provided in Gaussian with a step size of 0.01 amu$^{1/2}$ bohr. The potential energy along the MEP is shown as the dotted black curve in Fig. 2.

Calculations of minimum-energy geometries on the singlet and triplet PESs show that the product ($Fe(CO)_5$) has mainly singlet character and has a standard-state Gibbs free energy 25.4 kcal mol^{-1} below the reactant. The triplet surface (shown as the red dotted curve in Fig. 2) is essentially repulsive for all distances as the incoming CO ligand approaches the Fe atom, whereas the singlet surface is attractive between reactant and product, which agrees with the experimental observation.[61] The barrier occurs because the singlet PES is not yet significantly attractive at the Fe–C distances where the triplet PES is already rather repulsive. This is an example in which the saddle-point can be located only by including spin–orbit coupling in the calculation.

Based on the stationary point optimization on the spin-coupled surface, when spin–orbit coupling is considered, the transition state geometry is 0.5 kcal mol^{-1} higher than the reactant ($Fe(CO)_4$ + CO) on the mixed-spin PES with the corresponding Gibbs free energy of activation calculated to be 2.8 kcal mol^{-1}. A rough estimation of the reaction rate can be obtained by using the Eyring equation.[64] Assuming the transmission coefficient κ is 1 (*i.e.*, that the probability of a spin change is high, or equivalently that the reaction is electronically adiabatic), a Gibbs free energy of activation of 2.8 kcal mol^{-1} will result in a decrease in reaction rate at room temperature of about a factor of 100 compared to an activation-free reaction, which agrees reasonably well with the experimentally reported

Table 1 Geometric parameters of the transition state geometries for CO ligand associate to the $Fe(CO)_4$ complex. TSSMM: the transition state geometry optimized along mixed-spin MEP using the TSSMM. CP: the singlet–triplet crossing point geometry that appears in Fig. 2. MECP: minimum energy crossing point geometry reported in the literature using the MECP package

	α (°)	β (°)	γ (°)	r (Å)	r_{ax} (Å)	r_{eq} (Å)
TSSMM	130.9	152.8	97.6	2.685	1.871	1.837
CP	140.9	153.0	97.8	2.476	1.867	1.832
MECP	135[65]	165.8[3]	102.3[3]	2.557[3] 2.65[65]	1.901[3]	1.843[3]

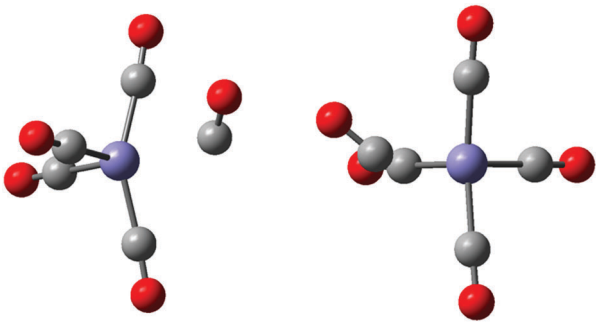

Fig. 1 Front and side views of the transition state geometries on the lowest mixed-spin PES for the association of CO ligand to the $Fe(CO)_4$ complex; O atoms are shown in red, C in grey, Fe in purple.

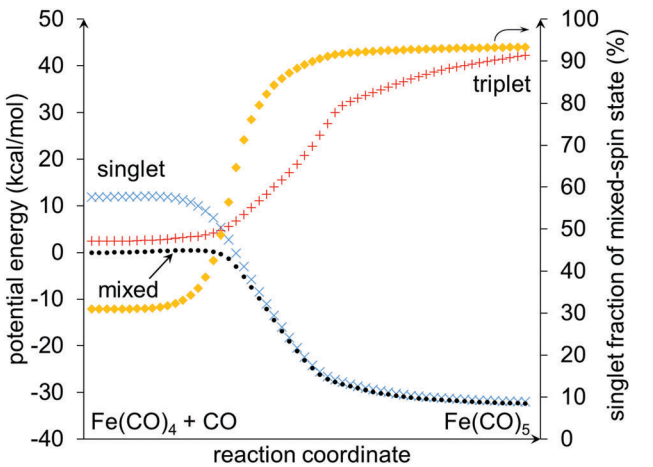

Fig. 2 Computed relative potential energy profiles along the mixed-spin MEP for the $Fe(CO)_4$ + CO system. The reactant ($Fe(CO_4)$ + CO) is chosen as the reference state. The black curve is the lowest singlet–triplet mixed-spin potential. The blue and red curves are the singlet and triplet potential curves along the mixed-spin MEP. The yellow curve is the singlet fraction of the mixed-spin state.

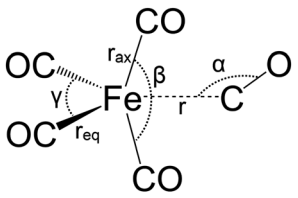

Fig. 3 Schematic structure of the transition state geometry for the association of CO ligand to the $Fe(CO)_4$ complex. Detailed geometric parameters are given in Table 1.

value[61] of a factor of about 500. The difference is due to the simple model used for evaluating the reaction rate as well as the application of a coupling constant derived from a representative geometry. Dynamical treatments that include both nonadiabatic and adiabatic traversal of the spin-coupling region could be used for a more complete treatment of the dynamics.[65–67]

4.2 Hydrogen elimination reaction of a tungsten model complex

Many redox reactions catalyzed by an organometallic complex involve a change of formal oxidation state of the transition metal and sometimes a possible change in spin state of the catalyst. Our second example concerns the α-H elimination reaction catalyzed by a model W complex:

$$W(CH_3)(n\text{-}C_3H_7)(OH)_2 \rightarrow W(H)(CH_3)(=CHC_2H_5)(OH)_2 \quad (R4)$$

This model complex is used to mimic an atomic-layer-deposited heterogeneous W catalyst with the support backbone replaced by two OH groups. During the H elimination reaction, the oxidation state of the W ion goes from +4 to +6. The product is coordinatively saturated and has a closed-shell singlet ground state, whereas the reactant is partially coordinated and has a triplet spin state.

Two sets of geometry optimizations were performed, one with and one without considering the effect of spin–orbit coupling. For calculations that ignore spin–orbit coupling, the reactant, product, and transition state geometries were optimized separately for both singlet and triplet spin states. The calculations were performed with the 6-31G* basis set[68,69] for the C, H, O atoms, and def2-TZVP basis set[62,63] for the W atoms; the latter basis set includes effective core potentials to treat 60 core electrons of the W atom.

Table 2 summarizes the computed relative energies of the reactants, transition states, and products optimized along the mixed-spin, singlet, and triplet PESs. We found that the singlet reactant lies 5.3 kcal mol^{-1} above the triplet reactant, whereas the singlet product lies 34.5 kcal mol^{-1} below the triplet product. Since the singlet spin state is energetically more stable than the triplet spin state for the product and less stable for the reactant, a crossing must occur between singlet and triplet PESs along the reaction pathway. Depending on the amount of energy required for the singlet and triplet PESs to approach each other, and the position along the reaction coordinate

Table 2 Computed electronic energies (kcal mol^{-1}) of the reactants, transition states, and products on the mixed-spin, singlet, and triplet PESs for the α-H elimination reaction catalyzed by the W model complex. The reference state is the reactant optimized on the mixed-spin PES

	Reactant	Transition state	Product
Mixed-spin geometry, mixed-spin energy	0.0	28.3	3.2
Mixed-spin geometry, singlet energy	13.1	30.0	3.9
Mixed-spin geometry, triplet energy	3.7	57.8	79.6
Singlet geometry, mixed-spin energy	9.6	30.9	5.9
Singlet geometry, singlet energy	11.2	31.9	6.3
Singlet geometry, triplet energy	27.4	59.9	75.8
Triplet geometry, mixed-spin energy	5.0	42.5	37.6
Triplet geometry, singlet energy	35.4	54.8	46.4
Triplet geometry, triplet energy	5.9	44.8	40.8

where the crossing occurs, the actual reaction barrier could be either higher or lower than those computed without considering the spin–orbit coupling. (For the reaction under consideration, the singlet transition state is 20.7 kcal mol^{-1} higher than the singlet reactant and 26.0 kcal mol^{-1} higher than the more stable triplet reactant. The triplet transition state is 12.9 kcal mol^{-1} higher than the singlet transition state.)

To determine whether the spin–orbit coupling affects the reaction kinetics, we studied the reaction by including the spin–orbit coupling using the method described above. Stationary points were optimized and the minimum energy path was calculated. The coupling constant χ was set to 302 meV. (Details of the determination the spin–orbit coupling parameter are provided in the ESI† for reference.) Based on the stationary point optimization on spin-coupled surface, when spin–orbit coupling is considered, the saddle point geometry is 28.3 kcal mol^{-1} higher than the reactant on the mixed-spin PES. The optimized transition state has mainly singlet character, whereas the reactant on the mixed-spin PES has mainly triplet character. The computed singlet energy of the mixed-spin transition state geometry is 1.7 kcal mol^{-1} higher than that of the mixed-spin energy, and the triplet energy computed at the mixed-spin transition state geometry is 29.5 kcal mol^{-1} higher than the mixed-spin energy. As for the reactant, the singlet and triplet energies of the mixed-spin reactant geometry are 13.1 and 3.7 kcal mol^{-1} higher than the corresponding mixed-spin energy, respectively. Even though the energy of saddle point geometry on the mixed-spin PES is 3.6 and 16.5 kcal mol^{-1} lower in energy than the saddle point geometries optimized on the pure singlet and triplet PESs without spin–orbit coupling, respectively, the energy of activation along the mixed-spin PES is 28.3 kcal mol^{-1}, and is 2.6 kcal mol^{-1} higher compare to the case where triplet reactant and singlet transition state are used to determine the activation barrier.

The optimized saddle point geometry on the mixed-spin PES has one imaginary frequency of 962i cm^{-1}. The results for the minimum energy path calculation are presented in Fig. 4. The black curve represents the singlet–triplet mixed-spin PES, the blue and red curves are pure singlet and pure triplet calculations at geometries along the mixed-spin minimum energy path. As shown in the figure, the singlet–triplet crossing occurs before

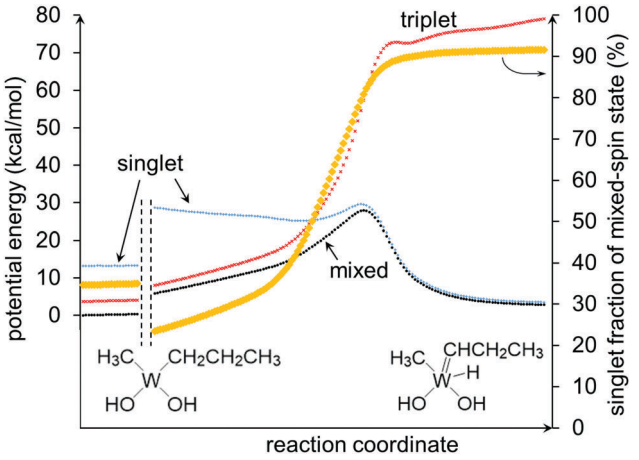

Fig. 4 Computed relative potential energy profiles along the mixed-spin MEP for the α-H elimination reaction catalyzed by the W model complex. The reactant ($W(CH_3)(C_3H_7)(OH)_2$) is chosen as the reference state. The black curve is the lowest singlet–triplet mixed-spin potential. The blue and red curves are the singlet and triplet potential curves along the mixed-spin MEP. The yellow curve is the singlet fraction of the mixed-spin state. The computed Gibbs free energy of activation for the reaction is 27.0 kcal mol^{-1}. Curves are truncated in the reactant direction (left side of the diagram) before they reach their asymptotic values, so the asymptotic region is displayed at the very left. Although the singlet potential energy curve rises as one moves toward reactant on the mixed-spin MEP, there is no saddle point in the reactant valley on the singlet MEP where the singlet electronic configuration changes from a closed-shell singlet to an open-shell state.

both the pure-spin transition states. The mixed-spin barrier that determines the kinetics of this α-H elimination reaction occurs where the electronic structure is primarily singlet in character. The energy of the crossing point where the blue and red curves intersect lies 7.0 kcal mol^{-1} above the mixed-spin surface at that geometry.

5. Conclusions

In this study, we present a new approximation method for locating stationary points on a mixed-spin potential energy surface in a simple way. The spin–orbit coupling between two spin states is incorporated into the geometry optimization by using a pre-defined coupling constant. Two reactions have been studied using the proposed method, in particular the CO association reaction with the $Fe(CO)_4$ complex and the α-H elimination reaction of a W model complex. For the CO association reaction, the singlet and triplet PESs of $Fe(CO)_4$ + CO cross at an Fe–C distance of 2.68 Å as CO approaches Fe within the equatorial plane of the bipyramidal structure. A reasonable Gibbs free activation barrier of 2.8 kcal mol^{-1} was obtained, which yields an estimated rate constant comparable to experimentally reported values. For the α-H elimination reaction of a W model complex, the singlet–triplet crossing occurs in the region close to the reactant along the reaction coordinates. The energy required for the singlet and triplet surfaces to intersect is lower than the activation barriers calculated without considering the spin–orbit coupling effect. The optimized saddle point geometry has mainly singlet character.

The method is shown to give a reasonable result at moderate computational cost. One has to be aware that in situations where spin–orbit coupling cannot simply be approximated by a constant value this approach will have quantitative errors, but it can still give useful structural information. By constructing the lowest mixed-spin PES along the reaction coordinate, useful insight into the reaction mechanism can be acquired and whether the kinetics of a spin-forbidden reaction is controlled by the nature of the spin-crossing or a conventional transition state can be determined.

Conflicts of interest

There are no conflicts to declare.

Acknowledgements

The authors are grateful to Kamal Sharkas and Zoltán Varga for helpful discussions. This work was supported as part of the Inorganometallic Catalysis Design Center, an Energy Frontier Research Center funded by the U.S. Department of Energy, Office of Science, Basic Energy Sciences under Award DE-SC0012702.

References

1 E. R. Davidson, *Chem. Rev.*, 2000, **100**, 351–352.
2 O. Wiest and Y. Wu, *Computational Organometallic Chemistry*, Springer-Verlag GmbH, Berlin, Heidelberg, 2012.
3 J. N. Harvey, in *Computational Organometallic Chemistry*, ed. T. R. Cundari, Marcel Dekker, Inc., New York, 2001, pp. 291–321.
4 B. A. Heß, C. M. Marian and S. D. Peyerimhoff, in *Modern Electronic Structure Theory*, ed. D. R. Yarkony, World Scientific, Singapore, 1995, pp. 152–278.
5 P. Gutlich, Y. Garcia and H. A. Goodwin, *Chem. Soc. Rev.*, 2000, **29**, 419–427.
6 C. M. Marian, in *Reviews in Computational Chemistry*, ed. K. B. Lipkowitz and D. B. Boyd, Wiley-VCH, Inc., Weinheim, Germany, 2001, vol. 17, ch. 3, pp. 99–204.
7 Z. Havlas, M. Kyvala and J. Michl, in *Computational Methods in Photochemistry*, ed. A. G. Kutateladze, CRC Press, Taylor & Francis Group, Vica Raton, FL, U.S.A., 2005, vol. 13, ch. 3, pp. 111–166.
8 R. Poli and J. N. Harvey, *Chem. Soc. Rev.*, 2003, **32**, 1–8.
9 C. M. Marian, *Rev. Comput. Chem.*, 2001, **17**, 99–204.
10 B. Yang and T. A. Manz, *Theor. Chem. Acc.*, 2016, **135**, 1–19.
11 D. G. Musaev and K. Morokuma, *J. Chem. Phys.*, 1994, **101**, 10697–10707.
12 M. C. Holthausen, A. Fiedler, H. Schwarz and W. Koch, *J. Phys. Chem.*, 1996, **100**, 6236–6242.
13 S. A. Decker and M. Klobukowski, *J. Am. Chem. Soc.*, 1998, **120**, 9342–9355.

14 K. M. Smith, R. Poli and J. N. Harvey, *New J. Chem.*, 2000, **24**, 77–80.
15 N. Koga and K. Morokuma, *Chem. Phys. Lett.*, 1985, **119**, 371–374.
16 A. Farazdel and M. Dupuis, *J. Comput. Chem.*, 1991, **12**, 276–282.
17 D. R. Yarkony, *J. Phys. Chem.*, 1993, **97**, 4407–4412.
18 M. J. Bearpark, M. A. Robb and H. B. Schlegel, *Chem. Phys. Lett.*, 1994, **223**, 269–274.
19 K. M. Dunn and K. Morokuma, *J. Phys. Chem.*, 1996, **100**, 123–129.
20 J. M. Anglada and J. M. Bofill, *J. Comput. Chem.*, 1997, **18**, 992–1003.
21 J. N. Harvey, M. Aschi, H. Schwarz and W. Koch, *Theor. Chem. Acc.*, 1998, **99**, 95–99.
22 J. N. Harvey and M. Aschi, *Phys. Chem. Chem. Phys.*, 1999, **1**, 5555–5563.
23 K. M. Smith, R. Poli and J. N. Harvey, *Chem. – Eur. J.*, 2001, **7**, 1679–1690.
24 J. Kim, T. K. Kim and H. Ihee, *J. Phys. Chem. A*, 2009, **113**, 11382–11389.
25 P. Å. Malmqvist, B. O. Roos and B. Schimmelpfennig, *Chem. Phys. Lett.*, 2002, **357**, 230–240.
26 B. O. Roos, P. Å. Malmqvist and L. Gagliardi, *J. Am. Chem. Soc.*, 2006, **128**, 17000–17006.
27 J. Kim, T. K. Hong, H. K. Kim, Y. S. Lee and T. K. Kim, *J. Chem. Theory Comput.*, 2013, **9**, 1087–1092.
28 D. G. Fedorov and J. P. Finley, *Phys. Rev. A: At., Mol., Opt. Phys.*, 2001, **64**, 042502.
29 C. A. Gaggioli, L. Belpassi, F. Tarantelli, D. Zuccaccia, J. N. Harvey and P. Belanzoni, *Chem. Sci.*, 2016, **7**, 7034–7039.
30 C. A. Gaggioli, L. Belpassi, F. Tarantelli, J. Harvey and P. Belanzoni, *Chem. – Eur. J.*, 2017, **23**, DOI: 10.1002/chem.201704608.
31 E. van Lenthe, J. G. Snijders and E. J. Baerends, *J. Chem. Phys.*, 1996, **105**, 6505–6516.
32 S. Luo, I. Rivalta, V. Batista and D. G. Truhlar, *J. Phys. Chem. Lett.*, 2011, **2**, 2629–2633.
33 C. A. Mead, *J. Chem. Phys.*, 1979, **70**, 2276–2283.
34 A. J. Stone, *Proc. R. Soc. London, Ser. A*, 1976, **351**, 141–150.
35 S. Matsika and D. R. Yarkony, *J. Chem. Phys.*, 2001, **115**, 2038–2050.
36 T. C. Allison, G. C. Lynch, D. G. Truhlar and M. S. Gordon, *J. Phys. Chem.*, 1996, **100**, 13575–13587.
37 D. G. Truhlar and C. A. Mead, *Phys. Rev. A: At., Mol., Opt. Phys.*, 2003, **68**, 32501.
38 O. Tishchenko, D. G. Truhlar, A. Ceulemans and M. T. Nguyen, *J. Am. Chem. Soc.*, 2008, **130**, 7000–7010.
39 G. Granucci, M. Persico and G. Spighi, *J. Chem. Phys.*, 2012, **137**, 22A501.
40 G. L. Cui and W. Thiel, *J. Chem. Phys.*, 2014, **141**, 124101.
41 B. N. Fu, B. C. Shepler and J. M. Bowman, *J. Am. Chem. Soc.*, 2011, **133**, 7957–7968.
42 M. Merchan, L. Serrano-Andres, M. A. Robb and L. Blancafort, *J. Am. Chem. Soc.*, 2005, **127**, 1820–1825.
43 L. Gagliardi and B. O. Roos, *Inorg. Chem.*, 2003, **42**, 1599–1603.
44 L. Gagliardi, M. C. Heaven, J. W. Krogh and B. O. Roos, *J. Am. Chem. Soc.*, 2005, **127**, 86–91.
45 P. J. Hay and T. H. Dunning, *J. Chem. Phys.*, 1977, **66**, 1306–1316.
46 T. Takayanagi, *J. Phys. Chem. A*, 2002, **106**, 4914–4921.
47 S. R. Langhoff, *J. Chem. Phys.*, 1980, **73**, 2379–2386.
48 B. Yang and D. G. Truhlar, *TSSMM – version 2017*, University of Minnesota, Minneapolis, MN, 2017.
49 M. J. Frisch, G. W. Trucks, H. B. Schlegel, G. E. Scuseria, M. A. Robb, J. R. Cheeseman, G. Scalmani, V. Barone, B. Mennucci, G. A. Petersson, H. Nakatsuji, M. Caricato, X. Li, H. P. Hratchian, A. F. Izmaylov, J. Bloino, G. Zheng, J. L. Sonnenberg, M. Hada, M. Ehara, K. Toyota, R. Fukuda, J. Hasegawa, M. Ishida, T. Nakajima, Y. Honda, O. Kitao, H. Nakai, T. Vreven, J. A. J. Montgomery, J. E. Peralta, F. Ogliaro, M. Bearpark, J. J. Heyd, E. Brothers, K. N. Kudin, V. N. Staroverov, T. Keith, R. Kobayashi, J. Normand, K. Raghavachari, A. Rendell, J. C. Burant, S. S. Iyengar, J. Tomasi, M. Cossi, N. Rega, J. M. Millam, M. Klene, J. E. Knox, J. B. Cross, V. Bakken, C. Adamo, J. Jaramillo, R. Gomperts, R. E. Stratmann, O. Yazyev, A. J. Austin, R. Cammi, C. Pomelli, J. W. Ochterski, R. L. Martin, K. Morokuma, V. G. Zakrzewski, G. A. Voth, P. Salvador, J. J. Dannenberg, S. Dapprich, A. D. Daniels, O. Farkas, J. B. Foresman, J. V. Ortiz, J. Cioslowski and D. J. Fox, *Gaussian 09 (Revision E.01)*, Gaussian, Inc., Wallingford, CT, 2010.
50 M. J. Frisch, G. W. Trucks, H. B. Schlegel, G. E. Scuseria, M. A. Robb, J. R. Cheeseman, G. Scalmani, V. Barone, G. A. Petersson, H. Nakatsuji, X. Li, M. Caricato, A. V. Marenich, J. Bloino, B. G. Janesko, R. Gomperts, B. Mennucci, H. P. Hratchian, J. V. Ortiz, A. F. Izmaylov, J. L. Sonnenberg, D. Williams-Young, F. Ding, F. Lipparini, F. Egidi, J. Goings, B. Peng, A. Petrone, T. Henderson, D. Ranasinghe, V. G. Zakrzewski, J. Gao, N. Rega, G. Zheng, W. Liang, M. Hada, M. Ehara, K. Toyota, R. Fukuda, J. Hasegawa, M. Ishida, T. Nakajima, Y. Honda, O. Kitao, H. Nakai, T. Vreven, K. Throssell, J. A. Montgomery Jr., J. E. Peralta, F. Ogliaro, M. J. Bearpark, J. J. Heyd, E. N. Brothers, K. N. Kudin, V. N. Staroverov, T. A. Keith, R. Kobayashi, J. Normand, K. Raghavachari, A. P. Rendell, J. C. Burant, S. S. Iyengar, J. Tomasi, M. Cossi, J. M. Millam, M. Klene, C. Adamo, R. Cammi, J. W. Ochterski, R. L. Martin, K. Morokuma, O. Farkas, J. B. Foresman and D. J. Fox, *Gaussian 16 (Revision A.03)*, Gaussian, Inc., Wallingford, CT, 2016.
51 G. te Velde, F. M. Bickelhaupt, E. J. Baerends, C. F. Guerra, S. J. A. Van Gisbergen, J. G. Snijders and T. Ziegler, *J. Comput. Chem.*, 2001, **22**, 931–967.
52 C. F. Guerra, J. G. Snijders, G. te Velde and E. J. Baerends, *Theor. Chem. Acc.*, 1998, **99**, 391–403.
53 E. J. Baerends, T. Ziegler, A. J. Atkins, J. Autschbach, D. Bashford, A. Bérces, F. M. Bickelhaupt, C. Bo, P. M. Boerrigter, L. Cavallo, D. P. Chong, D. V. Chulhai, L. Deng, R. M. Dickson, J. M. Dieterich, D. E. Ellis, M. van Faassen, L. Fan, T. H. Fischer, C. Fonseca Guerra, M. Franchini, A. Ghysels, A. Giammona, S. J. A. van Gisbergen, A. W. Götz, J. A. Groeneveld, O. V. Gritsenko, M. Grüning, S. Gusarov,

F. E. Harris, P. van den Hoek, C. R. Jacob, H. Jacobsen, L. Jensen, J. W. Kaminski, G. van Kessel, F. Kootstra, A. Kovalenko, M. V. Krykunov, E. van Lenthe, D. A. McCormack, A. Michalak, M. Mitoraj, S. M. Morton, J. Neugebauer, V. P. Nicu, L. Noodleman, V. P. Osinga, S. Patchkovskii, M. Pavanello, C. A. Peeples, P. H. T. Philipsen, D. Post, C. C. Pye, W. Ravenek, J. I. Rodríguez, P. Ros, R. Rüger, P. R. T. Schipper, H. van Schoot, G. Schreckenbach, J. S. Seldenthuis, M. Seth, J. G. Snijders, M. Solà, M. Swart, D. Swerhone, G. te Velde, P. Vernooijs, L. Versluis, L. Visscher, O. Visser, F. Wang, T. A. Wesolowski, E. M. van Wezenbeek, G. Wiesenekker, S. K. Wolff, T. K. Woo and A. L. Yakovlev, *ADF 2016, SCM, Theoretical Chemistry*, Vrije Universiteit, Amsterdam, The Netherlands, 2016.

54 E. Vanlenthe, E. J. Baerends and J. G. Snijders, *J. Chem. Phys.*, 1993, **99**, 4597–4610.

55 S. J. A. van Gisbergen, J. G. Snijders and E. J. Baerends, *Comput. Phys. Commun.*, 1999, **118**, 119–138.

56 F. Wang, T. Ziegler, E. van Lenthe, S. van Gisbergen and E. J. Baerends, *J. Chem. Phys.*, 2005, **122**, 204103.

57 A. Rosa, E. J. Baerends, S. J. A. van Gisbergen, E. van Lenthe, J. A. Groeneveld and J. G. Snijders, *J. Am. Chem. Soc.*, 1999, **121**, 10356–10365.

58 Y. Zhao and D. G. Truhlar, *J. Chem. Phys.*, 2006, **125**, 194101.

59 C. J. Cramer and D. G. Truhlar, *Phys. Chem. Chem. Phys.*, 2009, **11**, 10757–10816.

60 H. S. Yu, X. He and D. G. Truhlar, *J. Chem. Theory Comput.*, 2016, **12**, 1280–1293.

61 T. A. Seder, A. J. Ouderkirk and E. Weitz, *J. Chem. Phys.*, 1986, **85**, 1977–1986.

62 F. Weigend and R. Ahlrichs, *Phys. Chem. Chem. Phys.*, 2005, **7**, 3297–3305.

63 F. Weigend, *Phys. Chem. Chem. Phys.*, 2006, **8**, 1057–1065.

64 S. Glasstone, K. J. Laidler and H. Eyring, *Theory of Rate Processes*, McGraw-Hill, New York, 1941.

65 J. N. Harvey and M. Aschi, *Faraday Discuss.*, 2003, **124**, 129–143.

66 K. Morokuma, Q. Cui and Z. Liu, *Faraday Discuss.*, 1998, **110**, 71–89.

67 A. O. Lykhin, D. S. Kaliakin, G. E. dePolo, A. A. Kuzubov and S. A. Varganov, *Int. J. Quantum Chem.*, 2016, **116**, 750–761.

68 G. A. Petersson, A. Bennett, T. G. Tensfeldt, M. A. Allaham, W. A. Shirley and J. Mantzaris, *J. Chem. Phys.*, 1988, **89**, 2193–2218.

69 G. A. Petersson and M. A. Allaham, *J. Chem. Phys.*, 1991, **94**, 6081–6090.

